Chapter 5

Biosensing Based on Magneto-Optical Surface Plasmon Resonance

Sorin David, Cristina Polonschii, Mihaela Gheorghiu, Dumitru Bratu, and Eugen Gheorghiu

Abstract

In spite of the high analytic potential of Magneto Optical Surface Plasmon Resonance (MOSPR) assays, their applicability to biosensing has been limited due to significant chip stability issues. We present novel solutions to surpass current limitations of MOSPR sensing assays, based on innovative chip structure, tailored measurements and improved data analysis methods. The structure of the chip is modified to contain a thin layer of Co-Au alloy instead of successive layers of homogenous metals with magnetic and plasmonic properties, as currently used. This new approach presents improved plasmonic and magnetic properties, yet a structural stability similar to standard Au-SPR chips, allowing for bioaffinity assays in saline solutions. Moreover, using a custom-designed measurement configuration that allows the acquisition of the SPR curve, i.e., the reflectivity measured at multiple angles of incidence, instead of the reflectivity value at a single-incidence angle, a high signal-to-noise ratio is achieved, suitable for detection of minute analyte concentrations. The proposed structure of the MOSPR sensing chip and the procedure of data analysis allow for long time assessment in liquid media, a significant advancement over existing MOSPR chips, and confirm the MOSPR increased sensitivity over standard SPR analyses.

Key words Magneto-optic surface plasmon resonance, Magnetic alloys, Surface plasmon resonance enhancement, Affinity biosensor, Angle-resolved surface plasmon resonance, Fixed-angle surface plasmon resonance

1 Introduction

Surface Plasmon Resonance is a phenomenon that appears when a plane-polarized light is coupled, under total internal reflection (TIR) conditions, into a metal film at the interface between two media. The TIR conditions are met when the incident light beam intersects the interface between two adjacent media that have different refractive indices ($n_1 > n_2$) at an angle θ greater than the critical angle θ_c defined by Eq. 1 derived from the Snell law,

Avraham Rasooly and Ben Prickril (eds.), *Biosensors and Biodetection: Methods and Protocols Volume 1: Optical-Based Detectors*, Methods in Molecular Biology, vol. 1571, DOI 10.1007/978-1-4939-6848-0_5,

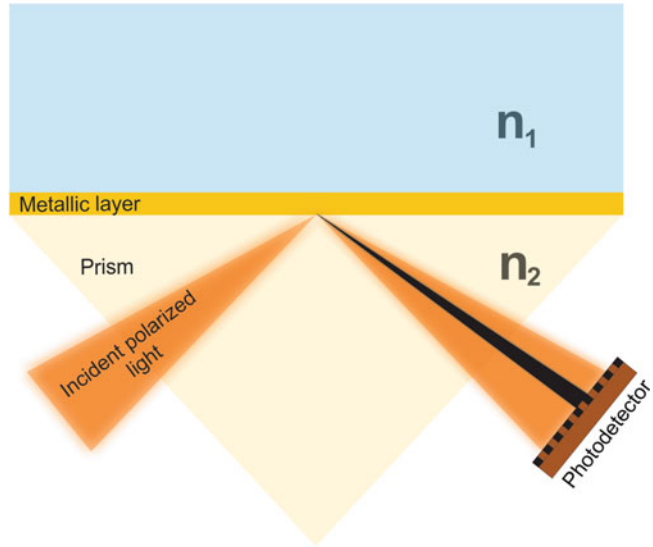

Fig. 1 Principle of surface plasmon resonance in Kretschmann configuration

$$\theta_c = \frac{n_2}{n_1} \tag{1}$$

where n_2 is the refractive index of the upper medium and n_1 is the refractive index of the lower medium and the light travels from n_1 toward n_2.

The coupling of the light into the metal film is done via a grating (Otto configuration) or a prism (Kretschmann configuration) [1]. In the following, only the Kretschmann configuration is considered.

Depending on the value of the incident light angle θ, the type of the plasmonic metal, and the refractive indices of the two media, the light interacts with the free electrons of the metal film and the energy of the photons is transferred resonantly to these electrons. A drop in the intensity of the reflected light is recorded by a suitable detector (e.g., a photodetector array) placed in the path of the reflected beam—Fig. 1 corresponding to the specific SPR angle. The dependency of the intensity of the reflected light over the incidence angle generates the SPR curve that has a dip minimum corresponding to the SPR angle, $\theta_{\min}$ (Fig. 1). According to Eq. 2 [2], the SPR angle depends on λ (the wavelength of the incident light), via n^*_m, the complex refractive index of the plasmonic layer and the values of the refractive indices of the media n_1 and n_2.

$$\sin\theta_{\min} = \sqrt{\frac{n_m^{*2} \times n_2^2}{\left(n_m^{*2} + n_2^2\right) n_1^2}}; n_m^* = n_m + i \times k_m. \tag{2}$$

Considering n^*_m and n_1 constant (as part of the measuring setup, for a given wavelength of the incident light), the SPR angle

depends exclusively on n_2—the refractive index of the upper medium. As such, due to their high sensitivity to local changes in the refractive index of the upper media [1], SPR biosensing assays are currently among the methods of choice to assess bioaffinity interactions at interfaces. For example, the minimum resolvable refractive index change for the SPREETA sensor (Texas Instruments Inc.) used in this chapter is 1×10^{-6} RIU (refractive index units) [3].

Nevertheless, there is a continuous strive to improve the sensitivity of the existing SPR analysis. Possible avenues for improvement include optimization of the plasmonic layer into a multilayered structure, improvement in the sensitivity of photodetectors [1], or signal modulation [4, 5]. Promising signal modulation approaches are based on the magneto plasmonic effects [6–8] by employing the transverse magneto-optic Kerr effect (TMOKE). The TMOKE occurs as a result of applying a magnetic field perpendicular to the propagation plane of the incident p-polarized light versus a surface with magneto-optical properties. This leads to modulation of the wave vector resulting in changes in the intensity of the reflected light [9]. The process lays the foundation of the novel magneto-optical SPR (MOSPR) method [10].

In the MOSPR approach the modulation of the reflectivity (i.e., SPR) curve is accomplished by applying an alternating transversal magnetic field, perpendicular to the propagation plane of an p-polarized beam of light [9] incident via a prism coupler, onto a sensor chip exhibiting both magnetic and plasmonic properties (so-called MOSPR chip [4]). MOSPR response measured at a single angle of incidence yields improved sensitivity to the refractive index changes of up to two orders of magnitude, compared to classical SPR assays, as substantiated by both theoretical and experimental studies [2, 9–12].

Important drawbacks of the technique are given by the technologically challenging MOSPR chip fabrication involving metallic multilayers or nanostructures (e.g., nanodiscs, nanocrystals) [6–8] and the intrinsic magnetostrictive effect [5] that causes ferromagnetic materials to change their shape or dimensions during the process of magnetization and adds further stability concerns. Indeed, this complex, multilayered structure of the MOSPR sensing chips is prone to induce a lack of stability when chips are exposed to (saline) liquid samples and, as a result, current highly sensitive MOSPR assays are mostly gas sensors [10, 12, 13].

To overcome this barrier, a multilayered chip comprising a thin film of amorphous Au-Co alloy, capped with a layer of Au (to allow further functionalization) with optimized structure for improved magneto-plasmonic properties, provides a powerful alternative. This structure, recently proposed, exhibits both plasmonic and magnetic properties, and proves excellent stability in (saline) liquid media [14].

In a further improvement, we used the optimized MOSPR structure in an *angle-resolved* MOSPR bioassay (that allows the evaluation of the reflectivity curve in a wider angular range, instead of the reflectivity at a single (fixed) angle of incidence as employed in most of the current SPR/MOSPR experiments [13]) and confirmed experimentally both increased sensitivity in comparison with the current SPR/MOSPR approaches and a high stability (similar to the one achieved with classic, gold-only, SPR chips) when addressing saline liquid samples.

2 Materials

2.1 Surface Chemistry

1. Bovine serum albumin (BSA), human IgG (HIgG), affinity isolated anti-human IgG (AHIgG), N-hydroxysuccinimide (NHS), 1-ethyl-3-(dimethylaminopropyl) carbodiimide (EDC), ethilenediaminetetraacetic acid (EDTA), and ethanolamine were purchased from Sigma–Aldrich (Germany).
2. (1-mercapto-11-undecyl)hexa(ethylene glycol)carboxylic acid was purchased from Prochimia Surfaces, Poland (*see* **Note 1**).
3. Surfactant P20 was provided by GE Healthcare.
4. Matching oil Immersol 518 F, $n_e = 1.518$ from Carl Zeiss.
5. *Aqua regia* HCl:HNO_3 3:1 mixture (*see* **Note 2**).
6. *piranha* solution H_2SO_4:H_2O_2 3:2 mixture (*see* **Note 3**) .

2.2 Preparation of Magneto-Optical Sensor Chip

1. Au pellets (99.999%), Co (99.99%) pellets, and Ti sputter target (grade 2) were purchased from Kurt J. Lesker USA.
2. N-BK7 glass wafers were purchased from Sydor Optics.
3. Kurt J. Lesker PVD 75 system with substrate heater, thermal evaporation sources, and reactive sputtering source for metallic layer deposition.
4. PSD–UV–plasma cleaner from Novascan Technologies, Inc.

2.3 Working Solutions

1. immobilization buffer: 10 mM acetate buffer pH 5.5.
2. running buffer: HBS-EP buffer (10 mM HEPES, pH 7.4, 150 mM NaCl, 3 mM EDTA, 0.005% Surfactant P20).

Ultrapure water (Millipore) was used throughout the preparations.

2.4 Measurement Setup

1. Fluidic assembly.
2. SPR module based on SPREETA sensor model TSPR1K23 and custom data acquisition board with appropriate software.
3. Electromagnet with power supply for applying the oscillating magnetic field.
4. PC for data saving and processing.

2.5 Fluidics Assembly

1. Injection pumps—Cavro XLP 600 Tecan Inc.
2. PTFE tubes ID 0.3 mm and fittings from Upchurch Scientific.
3. Polyether ether ketone (PEEK) slab micromachined as flow chamber.
4. PDMS silicone—Sylgard 184 from DowCorning as gasket between the flow chamber and the (MO)SPR chips.

3 Methods

3.1 Fabrication of MOSPR Chips

1. Substrates of BK7 glass (0.3 mm × 4 mm × 11 mm) are cleaned by successive sonication in water, acetone, and isopropanol and dried in a stream of nitrogen.
2. The substrates are exposed to ozone plasma for 10 min using a PSD-UV plasma cleaner.
3. Substrates are loaded in the pressure chamber of the PVD 75 system.
4. The pressure chamber is pumped to a pressure of approximately 2×10^{-6} Torr.
5. Samples are heated to 150 °C for degassing for 30 min using the substrate heating facility of the PVD 75.
6. Samples were rotated at 10 rot/min to ensure uniform coating. All the deposition processes were done at room temperature.
7. Thickness and deposition rate of the deposited layers are constantly monitored by a quartz crystal microbalance (QCM) inside the evaporation chamber of the PVD 75. The QCM works by measuring the changes in the oscillation frequency of a quartz crystal as a result of adsorption of materials on the crystal surface. The PVD 75 QCM is calibrated in terms of adsorbed material (taking into account the elastic properties of the material) and position in relation to the substrate.
8. A layer of Ti (4 nm) is first sputtered on the glass substrates for improving the adhesion of subsequent layers, at 5×10^{-3} Torr Ar pressure and 8 W/cm^2 (*see* **Note 4**).
9. Standard SPR chips are fabricated by evaporating 50 nm of Au onto the Ti modified substrates (*see* **Note 5**).
10. The Au and Co layers are thermally evaporated at rates of 0.5 Å/s and 3 Å/s respectively (*see* **Note 6**).
11. The Au-Co-Au tri-layers consist in a 26 nm Au, 6 nm Co layer, separated from the sensing surface by a 12 nm Au layer. An intermediate layer of 2 nm Ti is inserted between Au and Co to improve adhesion of the two metals.
12. The Au-Co alloy chips are fabricated by evaporating 30 nm layer of alloy Au-Co followed by 15 nm of Au. No intermediate Ti layer is used.

13. The Au-Co alloy is thermally evaporated at a rate of 0.5 Å/s from a single tungsten boat containing corresponding quantities of Au and Co to yield an alloy of 10% Co—volumetric ratio (588 mg Au and 27 mg Co). Alternative techniques for producing thin films of magnetic materials and alloys do exist and may be used for a better control of the film composition and structure. However, they have limitations in respect to costs (*see* **Note 7**), or material type (*see* **Note 8**) .

3.2 Chips Functionalization and Bioaffinity Assays

1. (MO)SPR are cleaned by immersion in *piranha* solution for 10 min and washed with deionized water and ethanol.
2. Cleaned (MO)SPR chips are functionalized by immersion in ethanol solution containing 1 mM of 11-PEG-COOH thiol for 3 h.
3. Functionalized chips are mounted in the flow chamber of the measurement setup and further modified with the ligand (HIgG) by amine coupling [15]:
   (a) A mixture of 100 mM NHS and 400 mM EDC is passed over the chip for 7 min to activate the carboxylic groups of the thiol.
   (b) The ligand (30 μg/ml) is injected for 30 min in 10 mM acetate buffer at pH 5.5 to promote electrostatic pre-concentration.
4. The modified surface is deactivated for 7 min with 1 M ethanolamine pH 8.6.
5. The deactivated surface is blocked and tested for nonspecific adsorption by injecting a solution of 1 mg/ml BSA in HBS-EP (10 min).
6. All the immobilization procedure is performed at a flow rate of 30 μl/min with HBS-EP as running buffer.

3.3 (MO)SPR Measurements and Data Processing

For classical SPR measurements the response is derived from the SPR curve as a function the angle for which the minimum of the reflectivity is recorded [1]. The reflectivity (R_{pp}) is obtained by normalizing the intensity of the measured reflected p-polarized light versus a reference signal (e.g., obtained using an s-polarized light or a solution with an SPR dip outside the measurement range of the device). As pinpointed by Eq. 2, the SPR angle (θ_{min}), depends on the refractive index of the media in the immediate vicinity of the sensing surface [1] and is determined most precisely if the reflectivity dip is the sharpest. Changes at the sensing surface, accompanied by a modification of the refractive index, cause a shift in the SPR angle that is used for label-free assessment of biomolecular surface interactions. This is the preferred mode of operation for real-time measurements having a linear dependence on the refractive index changes and with the amount of molecules accumulated

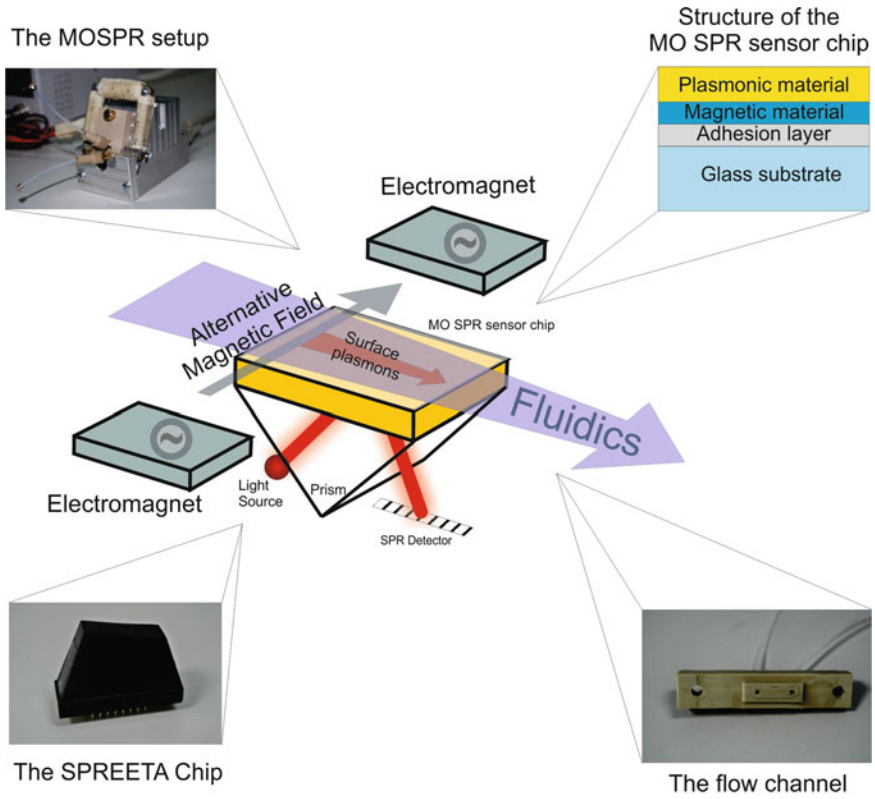

Fig. 2 The magneto optical SPR concept and schematic setup: electromagnet for transverse oscillating magnetic field application; tailored chips with magneto-plasmonic layers; top microfluidics; all system components were custom developed and built around an integrated illumination and detection Kretschman configuration as provided by a Spreeta module

on the surface [1]. Based on the full curve analysis, various data processing methods were developed to improve sensitivity, robustness against noise [16] and foster reduced time of analysis [17].

Figure 2 outlines the MOSPR concept. In brief, the measurement setup, described in more detail elsewhere [18], comprises:

- A SPR module.
- An external electromagnet with power supply for applying the alternating transverse magnetic field.
- A Flow Injection Analysis (FIA) type setup as fluidic assembly.

The SPR measurement module is based on a SPREETA sensor model TSPR1K23 (Texas Instruments USA). The FIA comprises a flow channel connected to an injection pump using PTFE tubes. The flow channel is made by micromachining a polyether ether ketone (PEEK) slab and a gasket of PDMS (Fig. 2). The data acquisition board is designed to give online access to whole curve measurements to allow calculation/extraction of the MOSPR data.

In the Kretschmann configuration [2] of the SPR module, the backside of the chip is illuminated using an embedded divergent p-polarized beam of light in a continuous range of incidence angles, spanning the 61–73° angular domain. The reflected light is assessed by a linear photo detector array comprising 128 pixels, each pixel measuring the intensity of the reflected light corresponding to a different angle of incidence. This allows for virtually simultaneous acquisition of angle specific reflectivity data, the whole SPR curve being measured in ~5 ms. The wavelength used is in the near infrared region of the spectrum (840 nm) and provides a rather sharp dip and large penetration depths for standard SPR Au chips measured in aqueous media. The relation between the individual pixels of the photo detector array and the corresponding angle of incidence θ, important especially when comparing SPR experimental data with numerical simulations provided by the Transfer Matrix approach, can be derived using the manufacturing parameters of the sensor. In the case of the TSPR1K23 sensor geometry, we find [14, 19]:

$$\theta = U_{\max} - (U_{\max} - U_{\min})/\text{PixelRange} \times \text{PixelPosition}, \quad (3)$$

where $U_{\max} = 73.427$ and $U_{\min} = 60.425$ are, respectively, the maximum and the minimum angle achieved in the SPREETA sensor, $PixelRange = 128$ is the total number of pixels of the photodetector array and *PixelPosition* is the value of the position of the individual pixel on the detector array, for which the angle θ is calculated.

For attaching tailored sensor chips to the SPREETA prism, a refractive index matching oil is used on the glass window of the sensor priory cleaned with *aqua regia* [20].

Calibration measurements are performed for each individual chip and relate the SPR responses (i.e., the variations of the measured SPR angle) to the effective refractive index values and involve assessment of water and glycerol solutions of various concentrations with known refractive index. The calibration process comprises injections in the measurement flow channel of solutions of known refractive index. The SPR response is recorded and the SPR angle is related to the refractive index of the calibration solution. Using several solutions with different refractive indices in the domain of interest, one can derive specific calibration curves for the SPR angle as a function of the refractive index of the solution in the flow channel. Further, the SPR analytic responses may be expressed as refractive index variations versus time (i.e., sensorgrams) or as concentrations of analyte (i.e., calibration curves).

MOSPR measurements are performed using tailored MOSPR sensor chips and an electromagnet placed transversal on the outside of the measurement chamber actuated with a sinusoidal voltage. The voltage is applied using a custom-built alternative current

source with a frequency domain of 0.1–100 Hz and a maximum current of 1 A. Field strengths of up to 5 mT (demonstrated as being sufficient for saturation of the magneto-optical chips [14]) were achieved using 120 mA, at the frequency of 0.3 Hz, current for electromagnet actuation.

In the typical experiment, reflectivity values are recorded when there is no magnetic field (R_{pp}) as well as for each direction of magnetization ($M+$) and ($M-$) when electromagnet actuation is performed.

Applying the alternating magnetic field did not create significant heating of the electromagnet nor had an effect over the SPR measurement on a classical gold surface, proving that there is no crosstalk between the magnetic field and the electronic and optic components of the SPREETA chip.

3.3.1 Extracting the MOSPR Data

The MOSPR signal is calculated from the reflectivity curves recorded in different states of magnetization of the MOSPR chip and is defined as $\Delta R_{pp}/R_{pp}$ [11]. Here, R_{pp} is the reflectivity (standard for SPR assays), obtained when not applying a magnetic field and ΔR_{pp} represents the difference between the reflectivity measured at one direction of magnetization ($M+$) and the reflectivity measured at the opposite direction of magnetization ($M-$). Figure 3a indicates the reflectivity curves in respect with magnetization as well as the corresponding ΔR_{pp}, R_{pp}, $\Delta\theta$ (the difference between the SPR angle measured at $M+$ and $M-$ respectively) and θ_{min} (the SPR angle measured with no magnetic field) data.

The MOSPR response is derived from the reflectivity values corresponding to a selected angle of incidence, as the variation of the reflectivity R_{pp} while switching the direction of the *in plane* magnetization of the sensor [10]:

$$\frac{\Delta R_{pp}}{R_{pp}(0)} = \frac{R_{pp}(M+) - R_{pp}(M-)}{R_{pp}(0)} \tag{4}$$

where $R_{pp}(M+)$ and $R_{pp}(M-)$ represent the reflectivities for the direction of the magnetization perpendicular to the propagation plane of the incident p-polarized light in both ways and $R_{pp}(0)$ represents the reflectivity without magnetization. In real measurements, ΔR_{pp} is obtained from the amplitude of the oscillations of the measured reflectivity (Fig. 3a). The MOSPR curve is defined as the variation of the $\Delta R_{pp}/R_{pp}$ versus the angle of incidence of the light.

As shown in Fig. 3b, for noise-free data a change in the refractive index of the media that yields a small reflectivity change in the SPR signal, determines a larger change in MOSPR signal. To this effect, an intermediary smoothing step is applied to the raw data.

3.3.2 Fitting Function of SPR Data

Reflectivity data for the entire angular range (SPR curves) are collected and fitted with a rational polynomial equation to achieve smoothing.

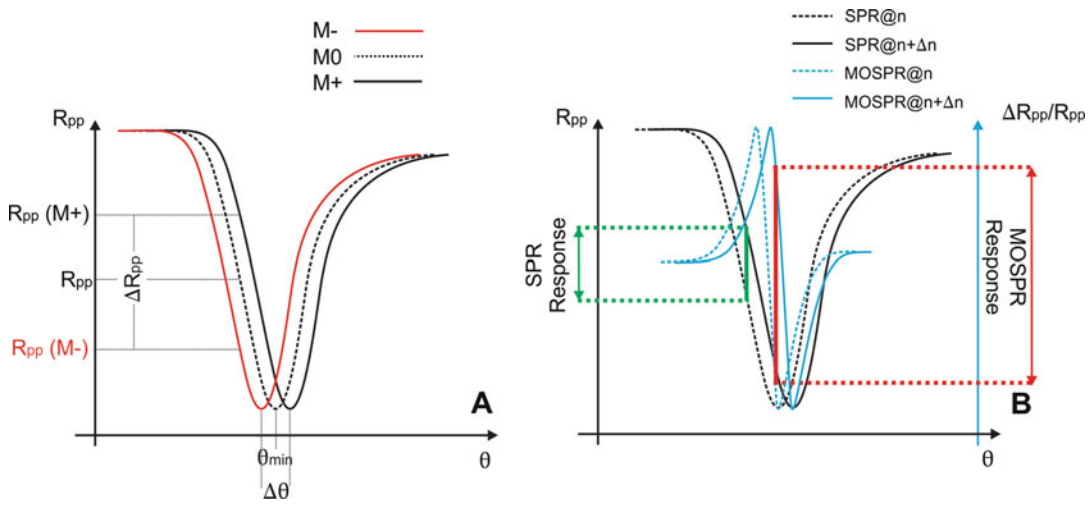

Fig. 3 (**a**) Representative parameters of the measured SPR curves used to derive the MOSPR data: R_{pp} the reflectivity value for a selected incidence angle; ΔR_{pp} corresponds to reflectivity differences between M+ and M− magnetization states, $\Delta\theta$ (the difference between the SPR angles for M+ and M− magnetization states) and θ_{min} (the SPR angle measured with no magnetic field). (**b**) Schematic plot showing ideal SPR (*black*) and MOSPR (*blue*) curves, as well as their variations corresponding to refractive index n (*dotted lines*) and $n + \Delta n$ (*continuous lines*), respectively

For fitting the experimental reflectivity data the following function is proposed [14, 21]:

$$f(x) = \frac{a_0 + a_1 x + a_2 x^2 + a_3 x^3 + a_4 x^4 + a_5 x^5 + a_6 x^6}{b_2 x^4 + b_1 x^2 + 1} \tag{5}$$

Here, x denotes the pixel position value and is related to the angle of incidence via Eq. 3, and $a_0 \div a_6$, b_1 and b_2 are the polynomial coefficients of the fitting function.

The good match of the rational polynomial function to the theoretical curve is presented in Fig. 4. A theoretical SPR curve is generated using the Transfer Matrix approach considering the literature optical constants of the standard structure comprising a glass prism (BK7 ε'=2.2801), covered with 4 nm Ti adhesion layer ($\varepsilon' = -1.7982; \varepsilon'' = 20.0613$) and 50 nm gold layer ($\varepsilon' = -30.2270$; ε''=2.1235) corresponding to $\lambda = 840$ nm. The theoretical curve is sampled to 128 points similar to the data received from the SPR detector (128 pixels). A $\chi^2 = 8.9 \times 10^{-9}$ residual error has been obtained for the fit, proving relatively insensitive to noise.

The fitted SPR curves provide corrected reflectivity values for each incident angle and are used to calculate the MOSPR curves. These smoothened MOSPR curves are used for further processing.

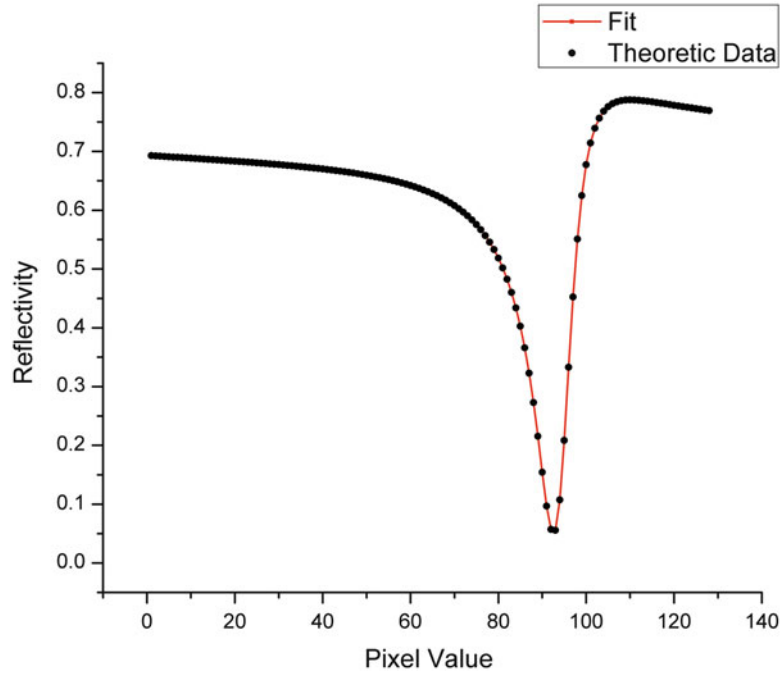

Fig. 4 Theoretical SPR curve for 50 nm layer of gold on glass with water on top (*black dotted line*) and the fit with the phenomenological, polynomial function (*red line*)

3.3.3 Sensitivity Comparison of MOSPR and SPR Sensors

The MOSPR responses are compared with SPR responses in terms of sensitivity and signal-to-noise ratio when analyzing the reflectivity at a given, single angle of incidence.

According to Eq. 4 the MOSPR signal is derived from $\Delta R_{pp}(\theta)/R_{pp}(\theta)$ data using the value of the reflectivity corresponding to a selected angle of incidence θ_s, chosen to yield the highest sensitivity. At this angle, the MOSPR curve (i.e., $\Delta R_{pp}/R_{pp}$ vs. incidence angle) presents the steepest slope [10]. We derive the θ_s angle by analyzing the derivative of the fitted SPR curve. Time series of full SPR curves are recorded, and then fitted with Eq. 5 and the reflectivity values (corresponding to θ_s) are plotted over time. Further, frequency (Fourier) analysis is performed to extract the amplitude of oscillations (corresponding to ΔR_{pp}) and their mean (corresponding to R_{pp}). MOSPR and SPR reflectivity responses derived from raw measurements directly from the detector corresponding to θ_s are presented in Fig. 5a while reflectivity responses calculated from fitted SPR curves are given in Fig. 5b. The SNR is calculated as the ratio between the response (SPR, MOSPR) and the corresponding root mean square deviation (RMSD – calculated on 100 data points). The comparison shows that fitting the curves (and hence reducing the noise) improves greatly the sensitivity (Fig. 5b). The sensitivity increase for the

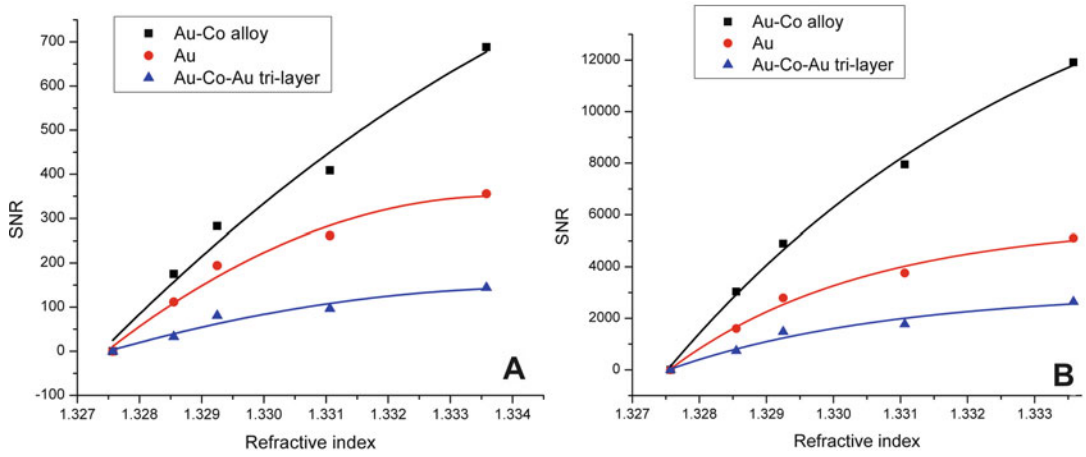

Fig. 5 (**a**) Signal-to-noise ratios for Au—SPR (*red*), Au-Co alloy—MOSPR (*black*) and Au-Co-Au tri-layer—MOSPR (*blue*) derived from raw reflectivity data for different refractive index solutions. (**b**) Signal-to-noise ratio for Au—SPR (*red*), Au-Co alloy—MOSPR (*black*) and Au-Co-Au tri-layer—MOSPR (*blue*) for solutions with different refractive indices—reflectivity values derived from fitted SPR curves

Au-Co alloy chip in respect to gold is 1.5-fold for raw reflectivity approach and reaches 2.5 times when using the reflectivity values derived from fitted SPR curves. In summary, Fig. 5a, b compare the SNR curves derived: (1) directly from the raw reflectivity data, and (2) when using the fitted SPR data. This highlights the advantage of our method in terms of improving on the SNR for both SPR and MOSPR assays.

3.4 MOSPR Chip Stability in Liquid Media

Stability of the MOSPR chips in physiological solutions is tested by exposure to a saline solution (e.g., HEPES buffer solution—HBS) while applying the oscillatory magnetic field. While the alloy shows no sign of destabilization (for virtually indefinite exposure, similar to regular Au sensor chips), in the case of Au-Co-Au tri-layer there is a significant exfoliation of the metallic film (Fig. 6a). Increase in the transparency of the film (observed under transmission microscopy Fig. 6a) further amplified with longer exposure confirms the conclusion of film exfoliation. In the same flow conditions and buffers, no modifications were observed in the cases of plain gold and/or Au-Co alloy (Fig. 6b).

3.5 Bioaffinity Assay

MOSPR assays of bioaffinity interactions are performed for the alloy-based MOSPR chip. Because of the corrosive effect of the saline buffers the Au-Co-Au tri-layers cannot be used even after surface modification and functionalization.

Affinity tests, using a model biomolecular interaction between human immuno-globulin G (HIgG) and Anti-HIgG in a direct assay [1], were performed. IgG is used as model analyte without restricting the generality of the method.

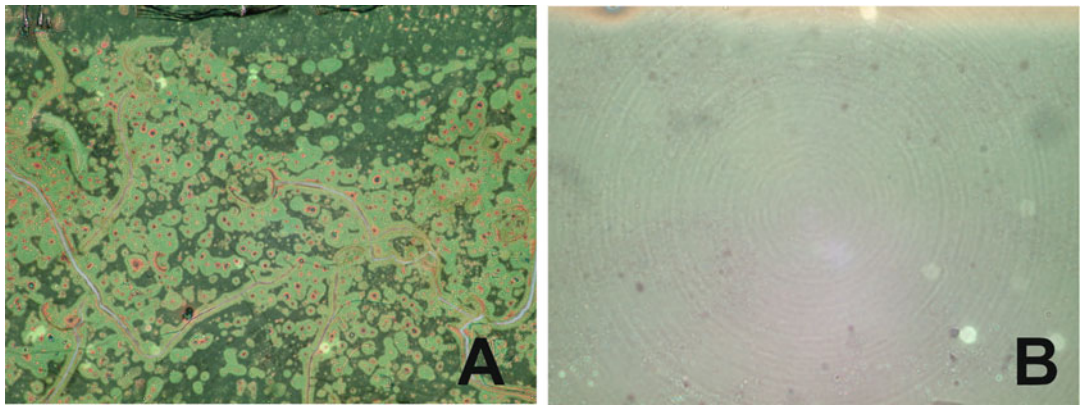

Fig. 6 Optical image of an Au-Co-Au tri-layer chip showing (**a**) pronounced corrosion in the areas exposed to saline solution in contrast with (**b**) non-corroded film

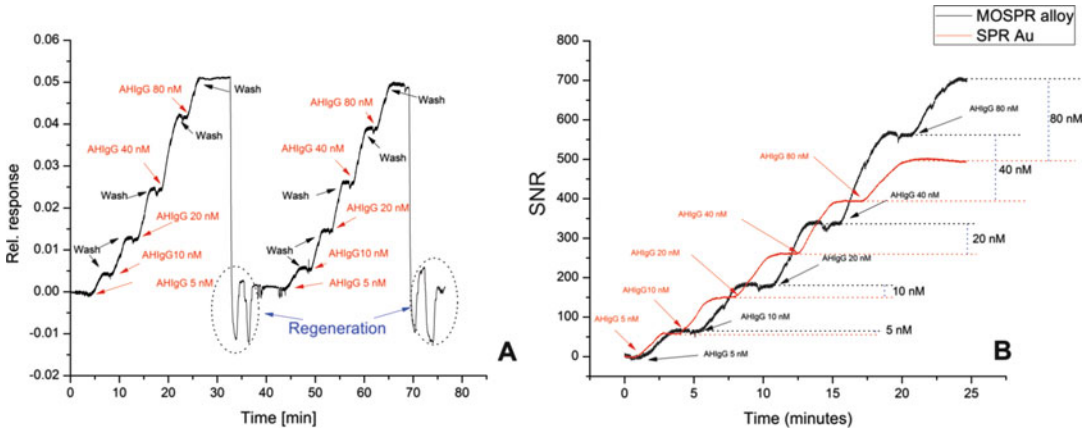

Fig. 7 (**a**) Relative reflectivity for several specific injections of Anti-HIgG (concentration range 5–80 nM) and two regeneration steps on the MOSPR Au-Co alloy chip. (**b**) Signal-to-noise ratio for specific MOSPR (for Au-Co alloy—*black*) and SPR (for Au chip—*red*) responses for several injections of Anti-HIgG

1. The sensor chip surfaces of Au-Co alloy are first functionalized using a carboxylated thiol and then further modified with HIgG via an amine coupling reaction.
2. The bioaffinity assay is performed at 100 µl/min, by injecting successively, for 2 min each, different concentrations of the analyte (A-HIgG) in the range 5–80 nM in HBS.
3. Each injection is followed by a washing step of 2 min to assess the binding level.
4. Surface is fully regenerated with two pulses of 10 mM glycine at pH 2 (2 min).

Several concentrations of Anti-HIgG (ranging from 5 to 80 nM) were injected consecutively over the sensor's surface and the response was recorded (Fig. 7a). The signal shows good

stability during the experiment: after regeneration (when the bioaffinity complexes are broken up and Anti-HIgG washed away) the signal always returns to initial baseline values, and comparable signals are obtained for multiple rounds of affinity binding (only two shown in Fig. 7a) demonstrating the good stability of the alloy in buffer and regeneration solutions.

The improvement of the SNR for the Au-Co alloy-based MOSPR assay as compared to the Au-based classic SPR assays (Fig. 7b) is evaluated by comparing the limit of detection (calculated as three times the standard deviation of blank) which is around 0.60 nM for MOSPR and 0.96 nM for the SPR assay, an improvement of 160% of the sensitivity of MOSPR over SPR assays.

3.6 Concluding Remarks

The proposed novel solutions, based on innovative chip structure, and tailored measurement and improved data analysis methods, surpass current limitations of MOSPR sensing assays and have been demonstrated to: (a) enable improved plasmonic and magnetic properties yet a structural stability similar to standard Au-SPR chips, allowing for bioaffinity assays in saline solutions, (b) detection of minute analyte concentrations (IgG is used as model analyte without restricting the generality of the method). The custom-designed MOSPR measurement configuration allows the quasi simultaneous acquisition of the whole SPR curve at high signal-to-noise ratios during long time assessment in liquid media, a significant advancement over existing MOSPR chips, and confirms the MOSPR increased sensitivity over standard SPR analyses.

4 Notes

1. Functionalization reagents are available from other commercial sources.
2. *Piranha* solution reacts violently with many organic materials and should be handled with extreme care.
3. *Aqua regia* preparation produces heat and poisonous vapors; it may react violently with many organic materials and should be handled with extreme care.
4. A chromium underlayer may also be employed.
5. A 50-nm-thick gold layer is optimal for this wavelength of incident light (840 nm). Optimal thickness varies with the wavelength of incident light.
6. Electron beam evaporation may be employed in place of thermal evaporation.
7. The sputtering technique may be used for depositing alloys [22–24]; however, magnetron sputtering magnetic material requires expensive magnetron guns with powerful magnets.

Moreover, manufacturing custom sputtering targets comprising gold alloys may have prohibitively high costs.

8. E-beam epitaxy may be also used for growing crystalline films with well-controlled magnetic properties but this is suitable/limited to substrates with crystalline structure [25].

Acknowledgments

The authors thank the Romanian Executive Unit for Higher Education, Research, Development and Innovation Funding for funding through grants PN II-ID-PCCE-2011-2-0075 and PN-II-RU-PD-2012-3-0467.

References

1. Schasfoort R, Tudos A (2008) Handbook of surface plasmon resonance. The Royal Society of Chemistry, Cambridge
2. Raether H (1988) Surface Plasmons on smooth and rough surfaces and on gratings. Springer, Berlin
3. Incorporated TI (2003) Spreeta on the sensitivity of spreeta. Solutions 2003:1–14
4. Sepúlveda B, Calle A, Lechuga LM, Armelles G (2006) Highly sensitive detection of biomolecules with the magneto-optic surface-plasmon-resonance sensor. Opt Lett 31:1085–1087
5. Regatos D, Sepúlveda B, Fariña D et al (2011) Suitable combination of noble/ferromagnetic metal multilayers for enhanced magneto-plasmonic biosensing. Opt Express 19:8336–8346
6. Armelles G, González-Díaz J (2008) Localized surface plasmon resonance effects on the magneto-optical activity of continuous Au/Co/Au trilayers. Opt Express 16:3112–3114
7. Temnov VV, Armelles G, Woggon U et al (2010) Active magneto-plasmonics in hybrid metal–ferromagnet structures. Nat Photonics 4:107–111. doi:10.1038/nphoton.2009.265
8. Belotelov VI, Kreilkamp LE, Akimov IA et al (2013) Plasmon-mediated magneto-optical transparency. Nat Commun 4:2128. doi:10.1038/ncomms3128
9. Zvezdin A, Kotov V (1997) Modern magnetooptics and magnetooptical materials. IOP Publishing Ltd, Bristol
10. Armelles G, Cebollada A, García-Martín A, González MU (2013) Magnetoplasmonics: combining magnetic and plasmonic functionalities. Adv Opt Mater 1:10–35. doi:10.1002/adom.201200011
11. Regatos D, Fariña D, Calle A et al (2010) Au/Fe/Au multilayer transducers for magneto-optic surface plasmon resonance sensing. J Appl Phys 108:054502. doi:10.1063/1.3475711
12. Manera MG, Montagna G, Ferreiro-Vila E et al (2011) Enhanced gas sensing performance of TiO2 functionalized magneto-optical SPR sensors. J Mater Chem 21:16049. doi:10.1039/c1jm11937k
13. Manera MG, Ferreiro-vila E, Cebollada A et al (2012) Ethane-bridged Zn porphyrins dimers in langmuir-Scha fer thin films: spectroscopic, morphologic, and magneto-optical surface plasmon resonance characterization. J Phys Chem C 116:10734–10742
14. David S, Polonschii C, Luculescu C et al (2015) Magneto-plasmonic biosensor with enhanced analytical response and stability. Biosens Bioelectron 63:525–532. doi:10.1016/j.bios.2014.08.004
15. Johnsson B, Löfås S, Lindquist G (1991) Immobilization of proteins to a carboxymethyldextran-modified gold surface for biospecific interaction analysis in surface plasmon resonance sensors. Anal Biochem 198:268–277. doi:10.1016/0003-2697(91)90424-R
16. Chinowsky TM, Jung LS, Yee SS (1999) Optimal linear data analysis for surface plasmon resonance biosensors. Sensors Actuators B Chem 54:89–97
17. Zhan S, Wang X, Liu Y (2011) Fast centroid algorithm for determining the surface plasmon resonance angle using the fixed-boundary method. Meas Sci Technol 22:025201. doi:10.1088/0957-0233/22/2/025201

18. David S, Gheorghiu E (2011) Towards an advanced magneto-plasmonic sensing platform. Adv Top Electr Eng (ATEE), 2011 7th International symposium 1:12–14
19. Gheorghiu M, David S, Polonschii C et al (2014) Label free sensing platform for amyloid fibrils effect on living cells. Biosens Bioelectron 52:89–97. doi:10.1016/j.bios.2013.08.028
20. Neuert G, Kufer S, Benoit M, Gaub HE (2005) Modular multichannel surface plasmon spectrometer. Rev Sci Instrum 76:054303. doi:10.1063/1.1899503
21. Polonschii C, David S, Tombelli S (2010) A novel low-cost and easy to develop functionalization platform. Case study: aptamer-based detection of thrombin by surface plasmon resonance. Talanta 80:2157–2164
22. Kahn D (1992) Magnetic properties and structure of cobalt hardened gold. SUR/FIN'92 1:305–341
23. Yang K, Clavero C, Skuza J (2010) Surface plasmon resonance and magneto-optical enhancement on Au–Co nanocomposite thin films. J Appl Phys 107:103924
24. Mattox D (2010) Handbook of physical vapor deposition (PVD) processing, 2nd edn. Elsevier, Inc., Berlin
25. Ferreiro-Vila E, Iglesias M, Paz E et al (2011) Magneto-optical and magnetoplasmonic properties of epitaxial and polycrystalline Au/Fe/Au trilayers. Phys Rev B 83:205120. doi:10.1103/PhysRevB.83.205120